Journal of Constructional Steel Research 158 (2019) 230–247

Contents lists available at ScienceDirect

Journal of Constructional Steel Research

Experimental and numerical assessment of steel beams under impact loadings

M. D'Antimo [a,*], M. Latour [b], G. Rizzano [b], J.F. Demonceau [a]

[a] University of Liège, ArGenCo Department, Belgium
[b] University of Salerno, Department of Civil Engineering, Italy

ARTICLE INFO

Article history:
Received 17 January 2019
Received in revised form 28 March 2019
Accepted 29 March 2019
Available online xxxx

Keywords:
Impact
Strain rate
FE model
Experimental tests
Steel structures

ABSTRACT

In order to provide a contribution towards a better understanding of the physical phenomena involved in the design of steel structures under impacts, the present paper focuses on the behaviour of simply supported beams in drop-weight tests analysing the possibility to model the response numerically through the FE approach. These tests represent an important benchmark to study the behaviour of steel members under impacts and they are usually necessary to provide an accurate modelling of structures under exceptional loading conditions. In the present study, nine experimental tests were conducted on simply supported beams analysing the response of members under the application of increasing weights and dropping heights. Subsequently, in order to evaluate the capabilities of the currently available FE modelling techniques a numerical model was calibrated in Abaqus/CAE verifying its accuracy against the experimental results. Different techniques and material constitutive laws were investigated with the aim to define the most appropriate modelling approach to account for strain rate effects. The numerical results were compared with the experimental ones, demonstrating that, when the strain rate effect is accounted for adequately in the material stress-strain law, the FE modelling is a valid tool to predict the response of steel beams under impact loads. Among the models considered, the Johnson-Cook and Cowper-Symonds constitutive laws provided the best accuracy in terms of peak displacement, peak force and residual displacement.

1. Introduction

The lack of clear rules to design civil engineering structures under exceptional actions has determined in the last decade an increase of the number of scientific investigations related to unconventional loads like blast, fire and impact [1–6]. If the static and seismic behaviour of structures and joints have already been widely investigated [7–11], [46, 47] impact and blast related problems, together with unconventional dynamic loads, are still open issues. An exceptional loading situation is an event which can lead to a severe dynamic loading of the structure and, eventually to its progressive collapse propagating from the initial failure of an element. To avoid progressive collapse, buildings need to be designed with an adequate plastic reserve in order to prevent or reduce the occurrence of disproportionate damages. The capacity of the structural system to redistribute unforeseen loads is called robustness and it is linked to the concepts of ductility and redundancy and thus, to the ability of the structural system to exhibit adequate deformation capacities under large displacements [12–16]. Two main reference codes for the design of structures under exceptional loads are: *i)* Part 1–7 of Eurocode 1 [17], containing the general guidelines to design structures under exceptional events and *ii)* the Unified Facilities Criteria (UFC-4-023-03) of the Department of Defense of USA (DoD) [18], which provide rules for advanced progressive collapse analyses.

Since dynamic loadings may lead to high strain rates and non-linear response, the dynamic nature of the loading and geometric/material non-linearity cannot be neglected. Often dynamic related effects may be accounted for in a simplified way through the adoption of simplified coefficients, called DIFs (Dynamic Increase Factors), which express the ratio between the dynamic and static resistance of the element. The DIF can be applied at the macroscale to obtain a global estimation of the dynamic effect (for the whole building or for the structural elements), or the same concept can be applied at the level of the material mechanical properties. The DIF depends on the intrinsic behaviour of the component and on the velocity of application of the load, according to the distribution of strain rates.

The knowledge of the dynamic behaviour of the structural members under dynamic loadings is a key point in the study of a structure under impact. However, real scale dynamic tests are expensive and sometimes difficult to control, requiring in general to rely also on FE simulations to investigate the complex physical phenomena involved. In order to

* Corresponding author.
E-mail addresses: m.dantimo@uliege.be (M. D'Antimo), mlatour@unisa.it (M. Latour), g.rizzano@unisa.it (G. Rizzano), jfdemonceau@uliege.be (J.F. Demonceau).

https://doi.org/10.1016/j.jcsr.2019.03.029
0143-974X/

simulate exceptional events, the dynamic nature of the actions needs to be taken into account both at the macro- and micro-scale level. In fact, since materials have a dynamic response substantially different from the static one, the mechanical non-linear behaviour and the strain rate sensitivity can influence the response of the whole structure in terms of resistance and ductility. Therefore, in order to understand the behaviour of structures under high strain rates, experimental and numerical studies on the response of basic elements, namely members and joints, have been performed during the last years [1,19–27]. Both beams and connections response under falling floor impact were investigated in [28]. Falling floors differ from a normal middle column removal due to the randomness of the impact location caused by the falling of the upper stories. In this work, the influence of the mass impact angle, the impact location and impact energy were studied. In [22,24] numerical models of beam-to-column joints under impact loading were developed in ABAQUS/Explicit or LS-DYNA and validated with experimental tests. Solid elements, different levels of complexity for the material behaviour laws and strain rates effects were considered. Yang et al. [24] performed drop weight tests on rigid joints demonstrating that FEM analysis are a valid tool for the evaluation of the behaviour of joints. However, several problems were encountered to estimate the peak impact force. Also in [20] beam to column connections were modelled using ABAQUS. In this case blast loadings were considered. Nevertheless, the FE model were validated by comparison with the results of dynamic cyclic tests.

In this paper, the objective is to compare different methodologies to account for the strain rate effect in numerical simulations and to estimate the value of the global DIF factors ([2,3,25,30]) for impacted beams in order to provide the basic tools to carry out dynamic analyses of steel structures accounting for the dynamic response of members. The simulations performed with FE models are calibrated on the results of experimental drop-weight tests on beams. The experimental investigation was carried out at the laboratoire de mécanique des Matériaux et des Structures (University of Liège) performing nine tests on IPE beams with impacting velocities ranging from 2.2 m/s to 7.6 m/s. Conversely, the FE study was carried out through the ABAQUS software package, modelling the experimental tests into a dynamic implicit framework. The behaviour of the material was calibrated considering different modelling approaches to account for the influence of the strain rate. In particular, two semi-empirical material models, Cowper-Symonds (CS) and Johnson-Cook (JC), and the simplified approach of the American code (DoD), were compared [2]. The coefficients of the two semi-empirical material laws were estimated using experimental results at high strain rates collected from the database of tensile tests carried out in [31]. Finally, a comparison with a material model disregarding the strain rate effects (NSR) is also given.

2. Experimental campaign

2.1. Experimental layout

The aim of the present work, as aforesaid, is to investigate the behavior of steel beams impacted at high loading rates through drop-weight tests, with the final goal to assess the capabilities of the currently available FE modelling techniques in reproducing adequately the experimental response of structural steel elements into an impact loading scenario. The experimental campaign has been conducted on two IPE 220 beams (Specimen 1 and Specimens 2 in Table 1) made of S275 steel. The first specimen has been submitted to six sequential impacts while the second to three sequential impacts, in both cases increasing the level of energy. The scheme corresponds to a three-point bending test as shown in Fig. 1a. The load is applied at the center of the beam through an impacting mass. In this type of free-fall tests, it is clear that the kinetic energy transferred to the specimen is the main input factor. It can be governed only through two parameters: the mass weight and the dropping height. Therefore, while the dropping height is usually limited by the geometry of the testing rig, the maximum weight applied, theoretically, can be adjusted according to the particular needs. In the specific case, two different masses

Table 1
Test matrix.

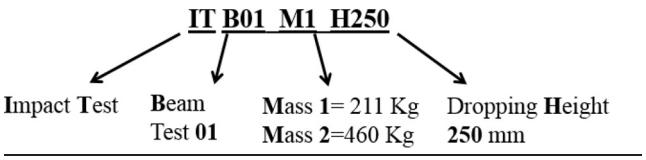

	Impact test	h [mm]	m [kg]
	Test CODE		
1st Specimen	ITB01 M1 H250	250	211
	ITB02 M1 H500	500	211
	ITB03 M1 H500	500	211
	ITB04 M1 H1000	1000	211
	ITB05 M1 H1000	1000	211
	ITB06 M1 H3000	3000	211
2nd Specimen	ITB07 M2 H250	250	460
	ITB08 M2 H500	500	460
	ITB09 M2 H1000	1000	460

falling from a fixed height through a specific dropping system have been employed, one of 211 kg (M1) and another of 460 kg (M2). The mass slides on tubular elements (Fig. 1a) which guide the motion before and after the collision. To drop the mass, a quick-release mechanism has been developed using a hook equipped with a spring. When the cable connected to the spring is pulled, the hook instantaneously releases the mass (Fig. 1b). A particularity of the testing rig is that the supports are designed to avoid the uplift of the beam when the mass rebounds. This is obtained introducing threaded bars connecting the plates of the supports to the beam.

All the measurements during the tests were performed using the Digital Image Correlation (DIC) technique. This is an image analysis method able to determine the absolute position of points on an object surface, in two or three dimensions. Two typologies of cameras were employed. A first type was used to detect the joint movements and the displacement of the mass in a stereoscopic framework. These cameras are called "Vision Research Phantom" (Fig. 2a) and have a high frequency of acquisition (3 kHz). In particular, to detect the movements in three dimensions, two Vision research Phantom cameras looking at the same object from two different positions were employed [32]. The second system of acquisition was used to record the movements of the mass only. This was composed by a couple of Basler A504k cameras. Differently from the other two devices, this acquisition system was working in a 2D framework with a frequency of 400 Hz. The available camera lenses (Zeiss 32 mm and Zeiss 50 mm) were able to cover a limited window and, therefore, only half specimen was monitored (Fig. 3). Therefore, with the help of a stochastic speckle pattern, glued on the specimen surface, the movements of several selected points were tracked during the tests (Fig. 2b).

The initial dropping height of the impacting mass was controlled through a laser system. This measure was taken from the top of the beam. The displacements, velocities and accelerations of the whole acquisition window were registered during the tests. Nevertheless, some points were covered by the mass in some frames, precluding the measurements in the upper part of the specimen. In the paper all the results are referred, just for the brevity, to point 1C (Fig. 3). This point was selected to focus mainly on the global deformation of the beam, which can be directly associated to the impact energy and it is not strictly dependent on the shape of the impactor.

In Table 2 a summary of the experimental tests is reported. All the specimens are identified with an alphanumeric tag describing the main features of the test, as herein reported:

2.2. Experimental results

Before executing the impact tests on the beams, coupons were extracted from the beam plates (flanges and webs) and static tensile

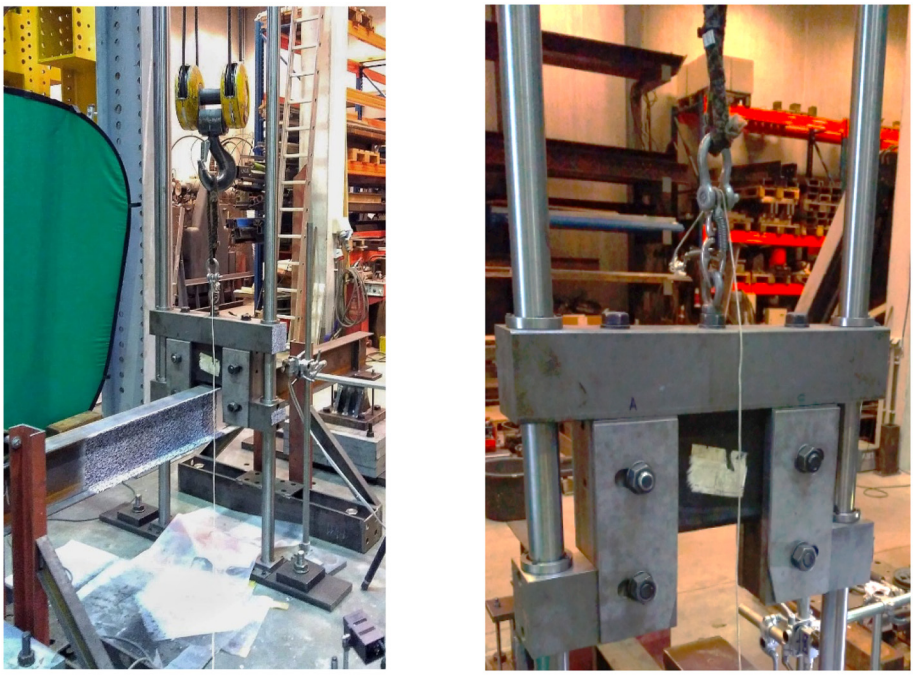

a) b)

Fig. 1. Detail of the impacting mass and test layout. a) Beam tests set-up. b) Detail of the quick-release mechanism (Mass"M1").

tests were performed to define the stress-strain curves of the materials under static loading conditions. These tests were carried out to calibrate accurately the material properties to be employed in the FE modelling. The results of the tensile tests are summarized in Table 2. The Engineering stress-strain curves (ENG) are reported below together with the True stress-True strain ones (TRUE), which are used in the next chapter for the Finite element simulations (Fig. 4).

As previously described, the experimental campaign is referred mainly to two set of tests. In a first phase, a sequence of impacts was applied to an IPE 220 beam with a mass of 211 kg (M1) dropped from heights ranging from 250 mm to 3000 mm. In a second phase, the beam was substituted, and another sequence of impacts was applied, increasing the size of the mass (M2 of 460 kg). In this second round of tests, the mass was dropped from heights ranging from 250 to 1000 mm. Unfortunately, due to strong vibrations, it was not possible to drop the mass from higher heights. In fact, the vibrations caused several problems to the acquisition system and an increase of loads in the tubular guides. Therefore, to preserve the equipment

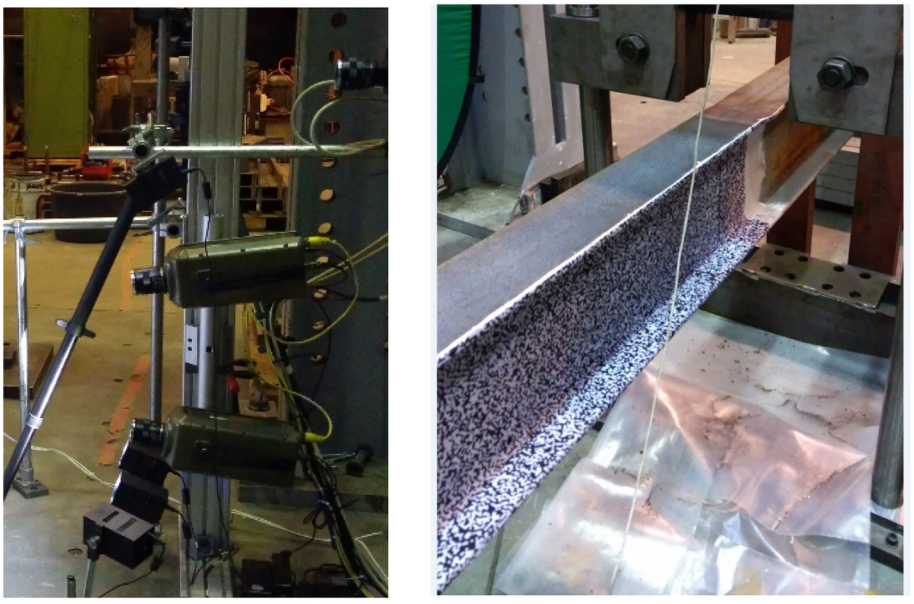

a) b)

Fig. 2. Acquisition system. a) High speed camera. b) Spekle pattern.

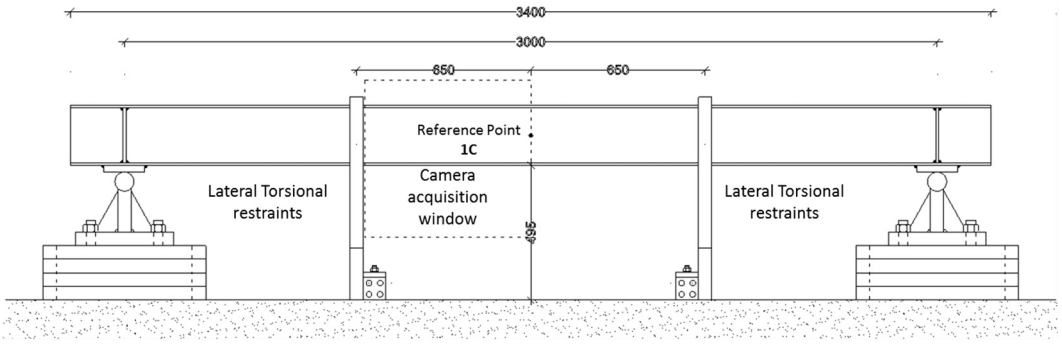

Fig. 3. Location of control point 1C for the beam specimens.

Table 2
Tensile tests results.

Coupon	b [mm]	t [mm]	R_{eH} [N/mm^2]	R_m [N/mm^2]	L_0 [mm]	L_u [mm]
Beam Flange Test 1	16.42	8.66	345.3	452.02	80	103.72
Beam Flange Test 2	16.48	8.42	350.1	451.4	80	102.06
Beam Web Test 1	20.57	6.23	387.2	480.8	80	101.77
Beam Web Test 2	20.47	6.19	357.2	460.8	80	105.37

t is the thickness of the tested specimen; R_{eH} is the upper yield strength; R_m is the ultimate tensile strength; L_0 is the gauge length; L_i is the length of prismatic portion of the specimen on which elongation is measured at a generic time during the test; L_u is the length after fracture;and A is percentage elongation.

from damages with the mass M2 it was decided to limit the dropping height to 1 m.

Images depicting the set-up of the first experimental campaign, with the mass M1 = 211 kg, are delivered in Fig. 5. The obtained experimental response, expressed in terms of time-displacement evolution of the control point 1C (Fig. 3) is reported in the charts delivered in Fig. 6. In the same figure, also an image depicting an enlarged view of the impacted area is reported.

The measurements performed with the camera acquisition system highlighted that the theoretical values of falling velocity of the mass do not correspond exactly to the actual values. In fact, owing to friction in the tubular guides and the air resistance, the velocity observed is

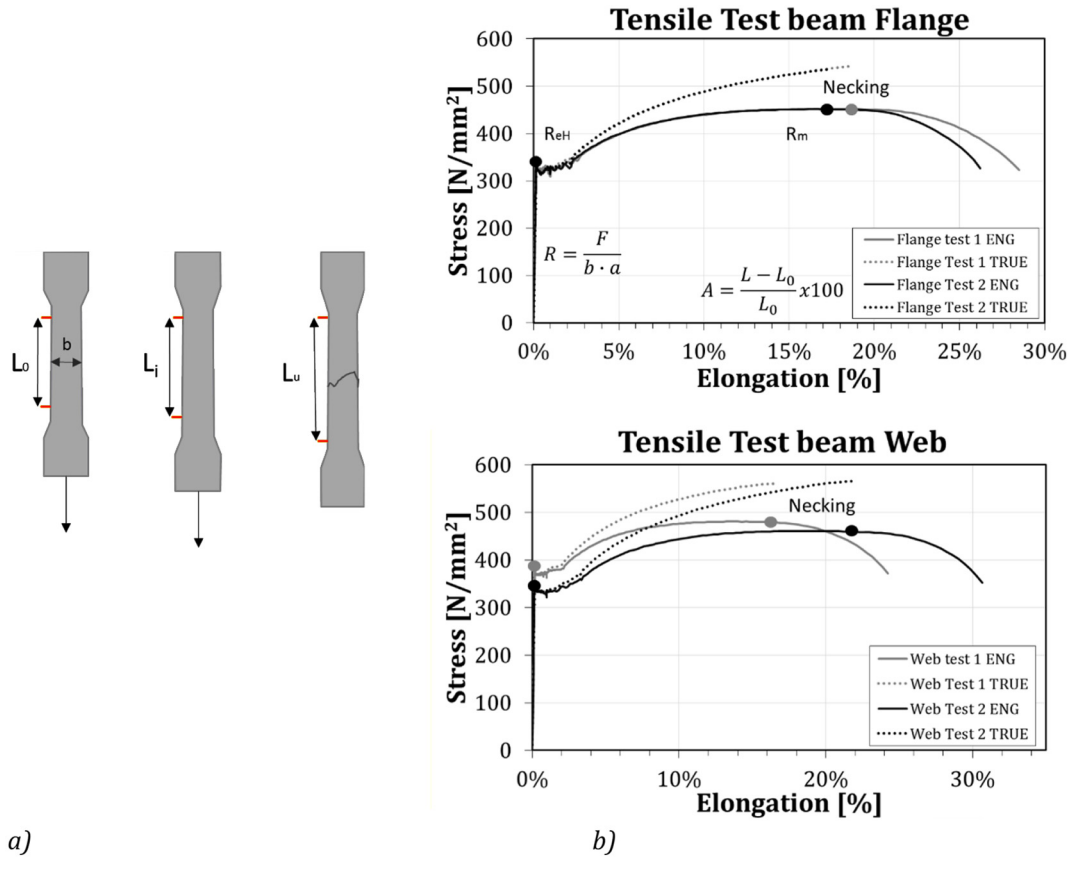

Fig. 4. Tensile tests results. a)Typical tensile test specimen. b) Material constitutive laws.

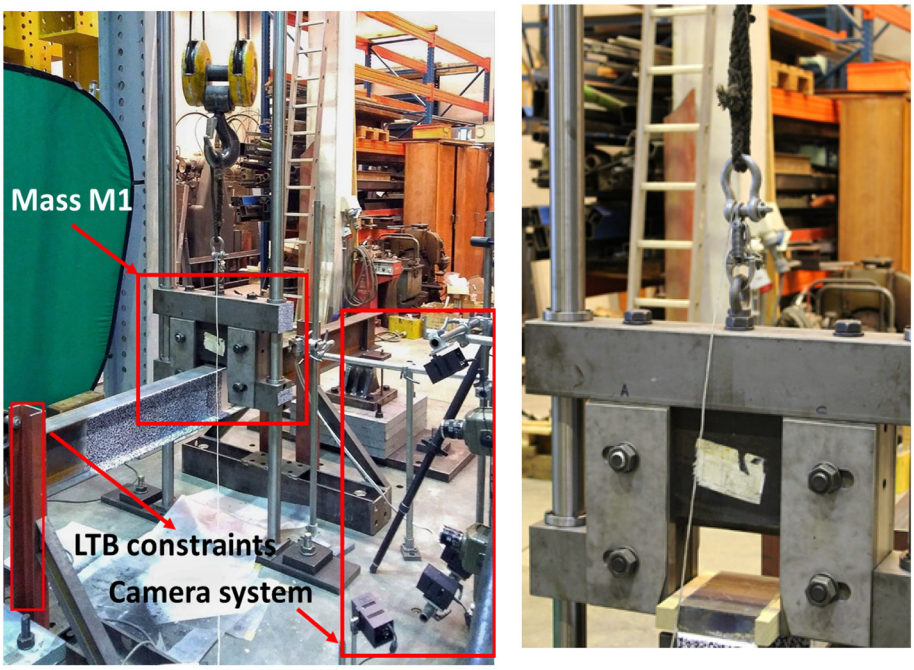

Fig. 5. Experimental set-up mass M1. a) Set-up with mass M1. b) Detail of the mass M1.

usually lower than the theoretical one. Therefore, while the theoretical values of the velocity and kinetic energy can be easily calculated as:

$$v_{theo,imp} = \sqrt{2gh} \tag{1}$$

$$E_{theo,imp} = \frac{1}{2} m v_{theo,imp}^2 \tag{2}$$

where g is the gravitational acceleration, m is the weight of the mass and h is the dropping height, the actual velocity in the instant of collision ($v_{act,imp}$) and the associated energy ($E_{act,imp}$) are normally lower. The theoretical and actual values are summarized in Table 3, showing that the lower is the dropping height, the higher is the scatter. In all the tests, the theoretical/actual ratio of the velocity ranged from 0.74 to 0.96. In the same table the values of the maximum (δ_{max}) and permanent (δ_{perm}) beam deflections are also reported. These displacements are referred to the deformed configuration of the beam at the beginning of each test. Therefore, to get the displacement of the beam referred to the initial configuration, the *i-th* maximum displacement ($\delta_{max,i}$) should be summed to the permanent displacements of all the previous impacts.

Of the six executed tests, unfortunately, some problems were encountered with the acquisition system during the tests three and four. Therefore, they are reported in the list mainly to provide the correct sequence of impacts, but no results are available. For the last two tests (i.e. Test 5 and Test 6), the development of plasticity in the beam was detected. In particular, permanent deformations equal to 4.76 mm (Test 5) and 25.01 mm (Test 6) were recorded. As expected, a correlation between dropping height and magnitude of the permanent deformations was observed.

After the end of the first sequence of tests, the mass was modified in order to try to introduce in the specimen higher impact energies. Therefore, the beam was substituted with a new one and the mass of 211 kg was replaced by a new steel element weighing 460 kg (Fig. 7). The same system of acquisition was employed and the same procedure to impact the beams was adopted. In this case, three tests were carried out, dropping the mass from heights of 250, 500 and 1000 mm. As aforesaid

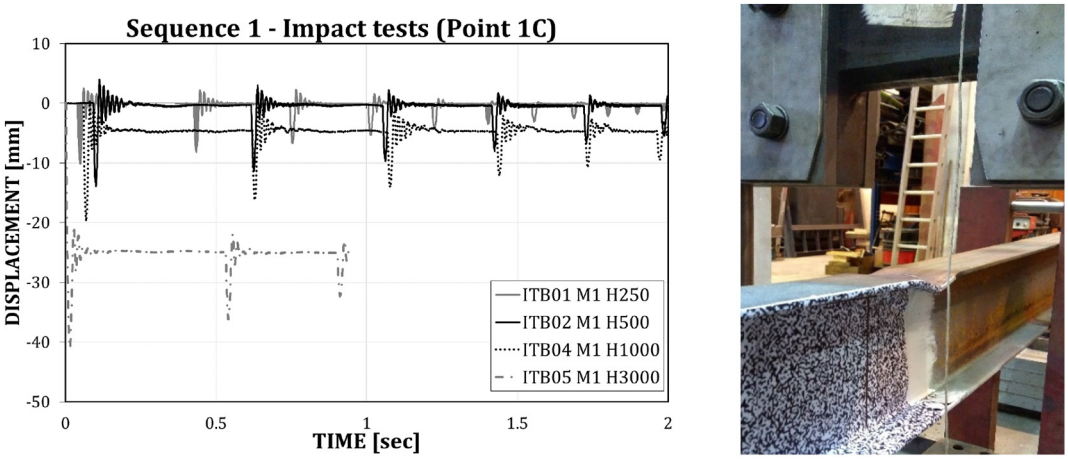

Fig. 6. Force-displacement of the control point (1C) and local deformation of the beam at the end of tests ITB06 M1 H3000.

Table 3
Impacts with mass M1.

Impact test M1 = 211 kg	h [mm]	$v_{theo,imp}$ [m/s]	$v_{act,imp}$ [m/s]	$E_{theo,imp}$ [J]	$E_{act,imp}$ [J]	$v_{theo,imp}/v_{act,imp}$	δ_{max} [mm]	δ_{perm} [mm]
ITB01 M1 H250	250	2.214	1.640	517.14	283.75	0.74	10.15	0
ITB02 M1 H500	500	3.132	2.720	1034.9	780.53	0.87	13.92	0
ITB03 M1 H500	500	3.132	2.766	1034.9	807.15	0.88	–	–
ITB04 M1 H1000	1000	4.429	3.836	2069.5	1534.6	0.87	–	–
ITB05 M1 H1000	1000	4.429	3.760	2069.5	1491.5	0.85	19.77	4.76
ITB06 M1 H3000	3000	7.622	7.310	6209.68	5637.5	0.96	40.99	25.01

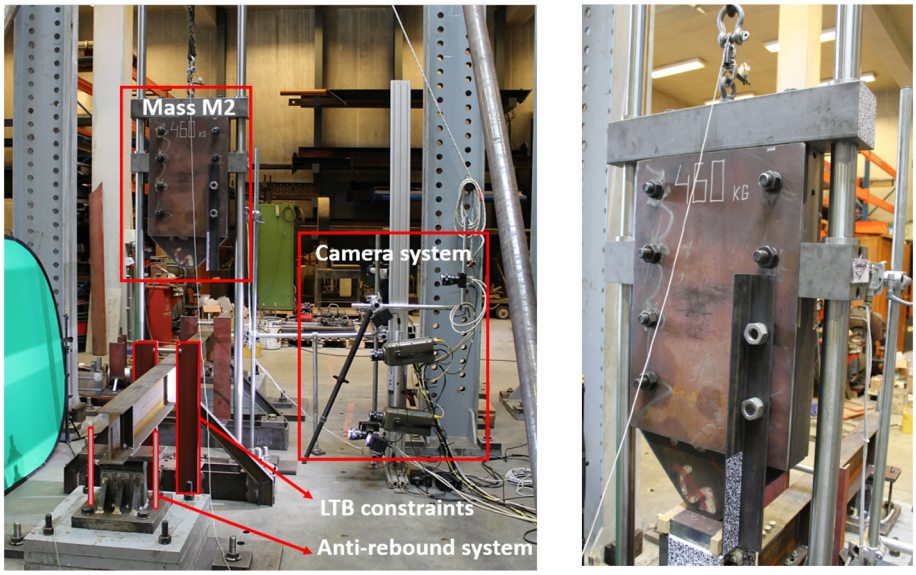

Fig. 7. Experimental set-up mass M2.

a further increase of the height was not possible because of the significant level of vibrations induced in the tubular guides. The results of this second round of tests are summarized in Table 4 following the same terminology previously introduced. Besides, the displacement-time curves are delivered in Fig. 8.

In order to better explain the observed behaviour of the specimens under impact, the results of one of the tests (IT-B09-M2-H1000) are described in higher detail, in the diagrams given in Fig. 9, reporting the displacement-time curve of control point 1C and the mass displacement-time curve together with the individuation of the different phases of the response. In the impact test there are mainly two bodies in motion: the beam and the mass. The beam initially stands still until it is impacted by the dropping mass which, in turn, before the impact is subjected only to a uniformly accelerated motion. After the collision, during a period Δt_1 the mass remains in contact with the beam. In this phase the two bodies move together, behaving as a single degree of freedom system in which part of the mass is uniformly distributed along the beam and part of the mass is lumped at the mid-point. In this time frame a first peak corresponding to the maximum displacement experienced by the beam is observed. After the end of period Δt_1 the mass rebounds achieving a new peak height in a time equal to $\Delta t'_2$ (this height is obviously lower than the initial dropping height due to the partial loss of kinetic energy) and, then, hits the specimen again after a further time $\Delta t''_2$ (Fig. 9b). Then, this separation and rebound mechanism repeats several times until the motion completely stops due to the full dissipation of the initial kinetic energy. This dissipation occurs due to hysteresis of steel, dissipation of the friction forces arising in the tubular guides and natural damping given also by the air resistance. At the end of the test, if the energy is such that the beam has undergone plastic deformations, a residual displacement remains.

When a perfect elastic impact takes place, the mass rebounds at a distance equal to the dropping height. Instead, in reality, as already evidenced, part of the energy is absorbed by the inelastic deformation of the impacted body. An overall measure of the level of inelasticity of the impact can be characterized by the so-called Coefficient Of Restitution *(COR)* (Eq. (3)), which expresses the ratio between the rebound velocity ($v_{rebound}$) and the impact velocity. For a perfectly elastic impact this coefficient assumes a value equal to 1.

$$COR = \frac{v_{rebound}}{v_{act,imp}} \leq 1 \tag{3}$$

Table 4
Impacts with mass M2.

Impact test M2 = 460 kg	h [mm]	$v_{theo,imp}$ [m/s]	$v_{act,imp}$ [m/s]	$E_{theo,imp}$ [J]	$E_{act,imp}$ [J]	$v_{theo,imp}/v_{act,imp}$	δ_{max} [mm]	δ_{perm} [mm]
ITB07 M2 H250	250	2.214	2.02	1128.1	938.5	0.91	15.08	0
ITB08 M2 H500	500	3.132	2.6	2256.3	1554.8	0.83	21.74	5.9
ITB09 M2 H1000	1000	4.429	4.09	4512.6	3856.8	0.92	33.14	16.78

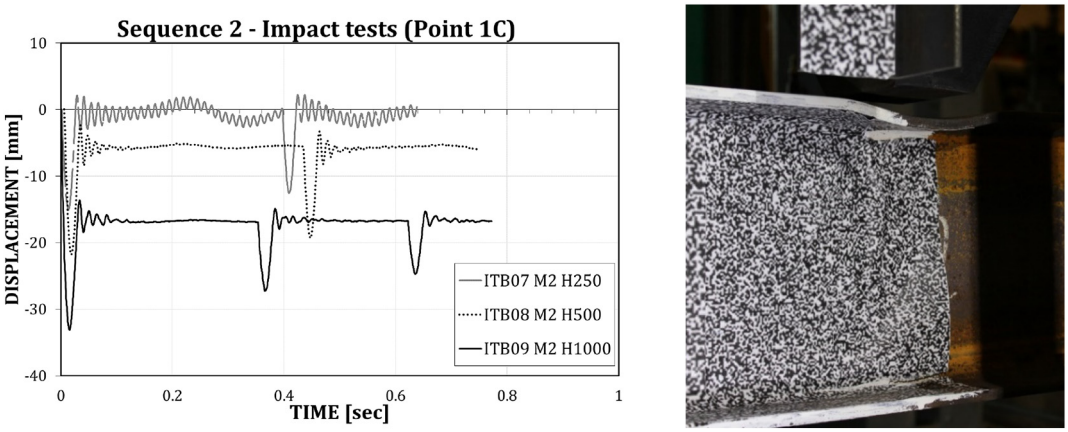

Fig. 8. Force displacement of the control point (1C) and local deformation of the beam.

This parameter has been measured for all the impacted beams, calculating the rebound velocity as the tangent velocity of the mass when the beam-mass separation occurs (green triangle in Fig. 9). In the experimental tests presented in this paper, the coefficient of restitution is varying from 0.99 to 0.30 (Table 5). The calculated values of the COR of the various tests show that the higher the impact energy, the lower the coefficient of restitution. This is clearly related to the contribution provided by the beam plasticity in the energy dissipation mechanism.

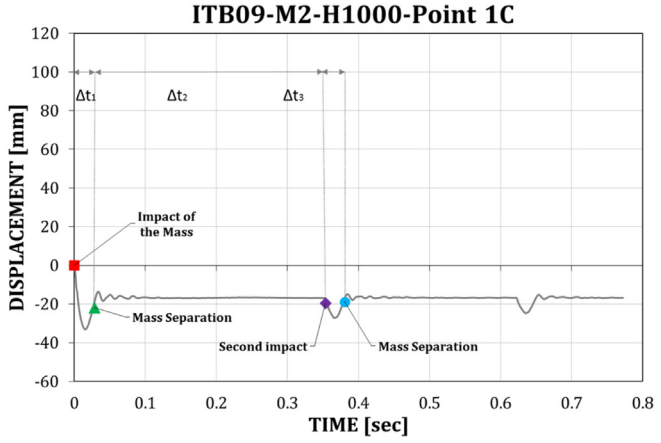

a)

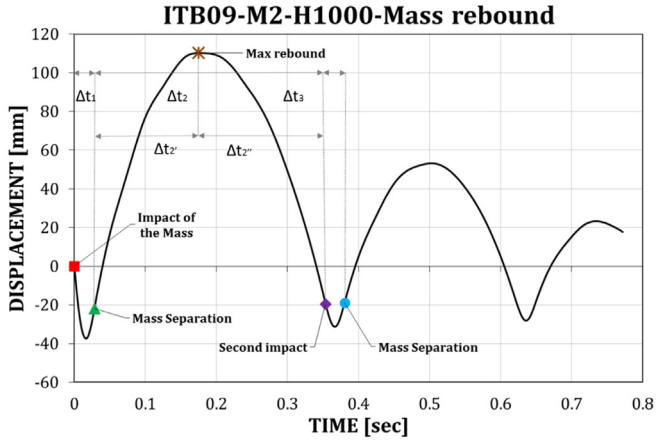

b)

Fig. 9. Displacement of control point in time (a) mass rebound (b) and identification of different time intervals.

In Fig. 10 some frames captured by the 3D camera system are reported, at some significant time steps, for the test ITB09 M2 H1000. From these images the selected points are tracked, and the displacements, velocities and acceleration are derived through image correlation. In the images, the white line represents the initial position of the beam (coincident with the beam lower flange) and the upper moving object with a white contour is the target attached to the mass. An arrow is indicating the direction of the movement.

In order to avoid damages to the available equipment the impact force was not directly recorded through load cells. Unfortunately, the laboratory at the ULg is not equipped with direct force measurers to be used in impact tests. Additionally, also strain gauges could not be used because the lab, currently, is not equipped with a high frequency data acquisition system. Nevertheless, the same procedure applied for the specimens of the research project ROBUSTIMPACT [31] was applied in this case.

Despite this, the impulse-momentum theorem was used to estimate the average force applied in the various tests. The impulse-momentum theorem is formally equivalent to the Newton's second law of motion and, as far as it does not rely on assumptions regarding the behaviour of the impacted body, it is valid both for elastic and inelastic impact. In the current case its application can be written as:

$$\overrightarrow{F_{IT}}\Delta t = m\Delta\vec{v} \rightarrow \overrightarrow{F_{IT}} = m \cdot \frac{\vec{v}_{act,imp} - \vec{v}_{rebound}}{\Delta t_1} \tag{4}$$

The forces at impact of the various tests, calculated according to the impulse-momentum theorem (F_{IT}) are reported in Table 6. It is interesting to note that the values estimated are fully consistent with the observed response. In fact, the ratio of the impact force over the plastic resistance of the beam is lower than one only when no residual deformations were detected at the end of the test. In Table 6, this ratio is also reported, considering that the plastic resistance of the beam is equal to about 132 kN.

Table 5
Coefficient of restitution.

TEST	M [kg]	h [mm]	$v_{act,imp}$ [m/s]	$v_{rebound}$ [m/s]	COR
ITB01 M1 H250	211	250	1.64	1.627	0.99
ITB02 M1 H500	211	500	2.766	2.281	0.82
ITB03 M1 H500	211	500	–	–	–
ITB04 M1 H1000	211	1000	–	–	–
ITB05 M1 H1000	211	1000	3.76	2.394	0.64
ITB06 M1 H3000	211	3000	7.31	2.201	0.30
ITB07 M2 H250	460	250	2.02	1.63	0.81
ITB08 M2 H500	460	500	2.6	1.835	0.71
ITB09 M2 H1000	460	1000	4.095	1.91	0.47

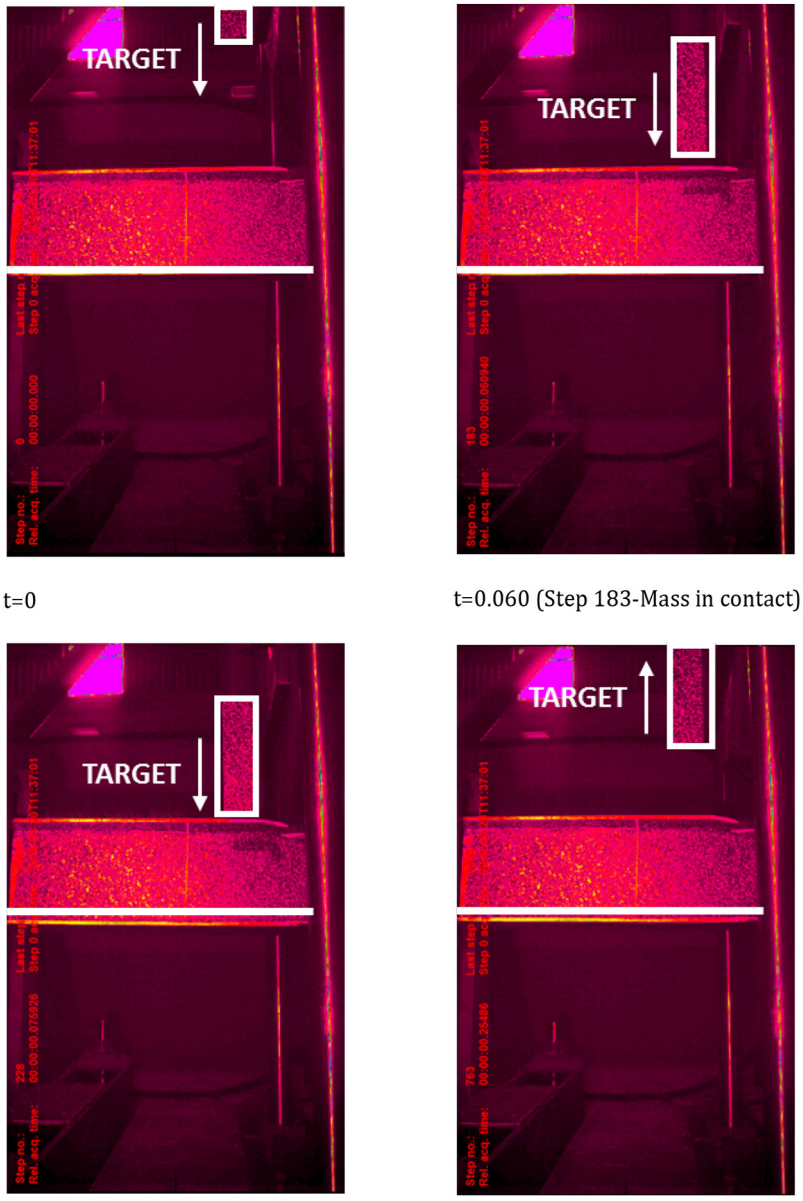

t=0 t=0.060 (Step 183-Mass in contact)

t=0.075 (maximum displacement specimen) t=0.25 (maximum rebound of the mass)

Fig. 10. Evolution of displacement at different time steps (images captured with 3D camera system).

As an alternative to the impulse-momentum theorem, the force associated to the impact was also estimated using a graphic approach (Fig. 11). This methodology is based only on the knowledge of the stiffness of the impacted beam and on the maximum and permanent values of the deflection [30].

Table 6
Estimation of the impact force: impulse theorem and graphic method.

Test	M [kg]	h [m]	$v_{act,imp}$ [m/s]	F_{IT} [kN]	F_{GR} [kN]	F_{IT}/F_{pl}	F_{GR}/F_{pl}
ITB01 M1 H250	211	250	1.640	82.8	100.0	0.62	0.75
ITB02 M1 H500	211	500	2.766	120.6	137.2	0.91	1.03
ITB05 M1 H1000	211	1000	3.760	149.9	149.2	1.13	1.13
ITB06 M1 H3000	211	3000	7.310	167.4	157.5	1.26	1.19
ITB07 M2 H250	460	250	2.020	122.9	148.7	0.93	1.12
ITB08 M2 H500	460	500	2.600	161.2	156.2	1.22	1.18
ITB09 M2 H1000	460	1000	4.095	176.5	161.3	1.33	1.22

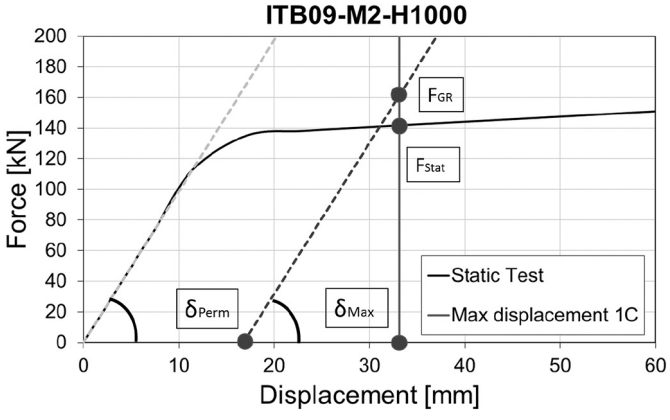

Fig. 11. Graphic estimation of the DIF.

Table 7
Dynamic increase factors for the inelastic impacts.

Impact test	δ_{max} [mm]	δ_{perm} [mm]	Beam stiffness [N/mm]	F_{Stat} [kN]	F_{IT} [kN]	F_{GR} [kN]	DIF_{IT}	DIF_{GR}
ITB05 M1 H1000	19.77	4.76	9860	137.5	149.9	149.2	1.09	1.08
ITB06 M1 H3000	45.75	29.77	9860	144.2	167.4	157.5	1.16	1.09
ITB08 M2 H500	21.74	5.9	9860	138.1	161.2	156.2	1.17	1.13
ITB09 M2 H1000	39.04	22.68	9860	141.5	176.5	161.3	1.25	1.14

Starting from the magnitude of the impact forces determined through the impulse-momentum theorem or through the graphic approach, the experimental values of the DIFs for the impacted beams were also calculated. The "equivalent" static resistance associated to each test was simply derived starting from the knowledge of the static force-displacement curve of the beam, which was obtained through the FE model described in next section.

The results are delivered in Table 7 reporting the experimental values of the DIFs for the four inelastic impacts. It is possible to observe that the DIFs derived with the two methodologies are similar. The scatter is, in fact, always lower than 10%. The static force given in the table is that associated to the level of displacement achieved in the impact test. This is always slightly different due to the occurrence of strain-hardening phenomena.

3. Numerical simulation of impact on simply supported beams

In order to evaluate the capabilities of the currently available FE modelling techniques in reproducing the behaviour of steel members under impact, a numerical model of the experimental tests was built in Abaqus/CAE. The accuracy of the developed model has been verified against the experimental results previously presented. Different constitutive laws were considered with the aim to define the most appropriate material model to account for the effects of strain rates. The FE model wants to reproduce the laboratory tests as accurately as possible, employing a 3D approach developed in a dynamic implicit framework. In the next sections, the main features of the modelling and of the employed material models are presented assessing, subsequently, the obtained accuracy.

3.1. FE model definition and modelling hypotheses

The numerical model was built, as above said, in a 3D environment, using three-dimensional hexahedra (brick) elements C3D8. The choice of the typology of elements was driven by the presence of complex non-linear phenomena involving contacts, plasticity and plastic deformations. In a first step of analysis the mesh sensitivity was investigated. To this scope, the FE model was developed both with a refined mesh, with 3 elements in the thickness of the beam flange, and with a coarser mesh providing only one element through the beam flange thickness. However, aside from a lower accuracy of the simpler model in reproducing the local deformation in the impacting area, the predictions of the two models were very similar in terms of global response. The satisfactory level of accuracy obtained also with the simpler model is mainly due to the type of finite element adopted, which is a 8-node hexahedra brick with full integration. After this preliminary phase of analysis, it was decided to refine the mesh at the beam centre, where the effects of the impact are higher, and three elements were introduced in the thickness of the flange. Moreover, since global and local buckling phenomena may occur in the beam, linear elements with full integration were used because they are both reliable and effective as already suggested in [33]. Overall the mesh was composed of 51,209 elements and after a sensitivity study, in order to detect also the local deformation of the beam under the impactor, the mesh in Fig. 12 was chosen.

The boundary conditions replicated the same support conditions outlined in the laboratory, simulating the three-point bending scheme, with the beam supported at the ends by rollers with unrestrained axial translations (Fig. 13) [34]. The mass was modelled as a 3D discrete rigid body with an isotropic inertia and it was meshed using rigid elements. Tie constraints were used to connect the stiffeners to the beam. A surface to surface contact was introduced between the dropping mass and the beam, with a "hard contact" definition in the normal direction. The dynamic implicit solver was selected for the impact simulation. In general, the implicit method may encounter some difficulties in achieving convergence for very complex modelling, but it was preferred in the present problem because it is an unconditionally stable method using a full Newton iterative solution. The impactor was placed initially directly in contact with the tested beam, assigning to the mass the value of the initial velocity as reported in Tables 3 and 4 ($v_{theo,imp}$).

The damping ratio is an important factor in the performed analyses because it governs the decay of the motion and the response of the beam in the free vibration phase. This parameter was introduced through a mass proportional definition of the damping matrix. Generally speaking, Abaqus/CAE allows to define the damping matrix according to the classical Rayleigh model, which is based on a combination of mass and stiffness proportional damping. With this model, the damping ratio of the i-th mode of vibration (ξ_i), characterized by the

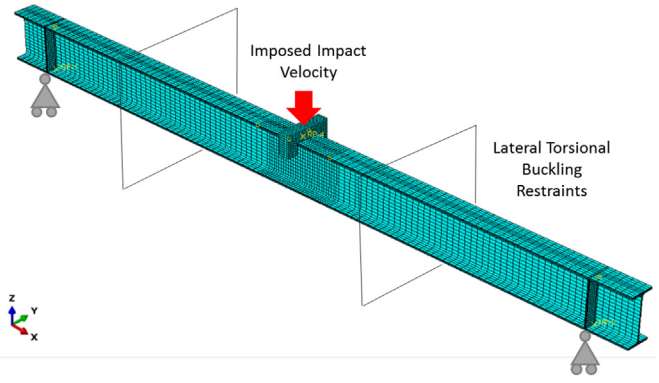

Fig. 12. FE model of the beam.

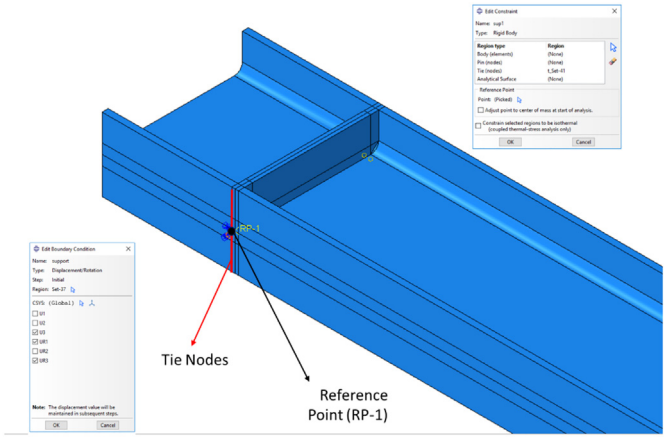

Fig. 13. Definition of the beam end supports.

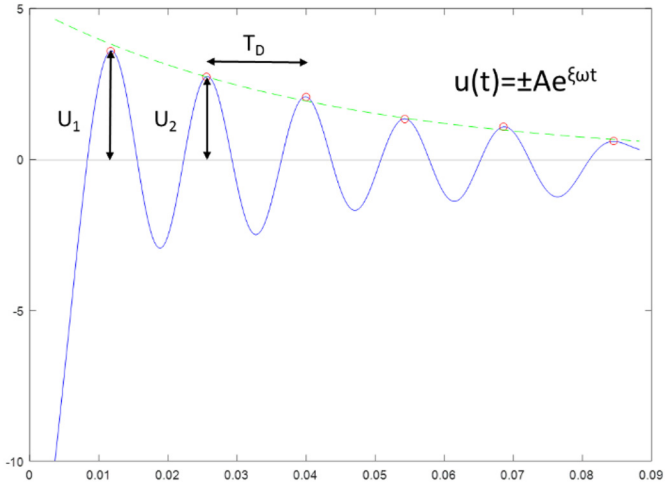

Fig. 14. Determination of the signal decay.

Table 8
Mass proportional coefficient.

Impact test	$\omega_{1,n,exp}$ Hz	$\xi_{1,\,exp}$	α_{exp}
ITB01 M1 H250	509	0.056	57
ITB02 M1 H500	481	0.055	52.91

natural frequency $\omega_{n,\,i}$, is defined through two constants (α and β), as follows:

$$\xi_i = \frac{1}{2\omega_{n,i}}\alpha + \frac{\omega_{n,i}}{2}\beta \tag{5}$$

Clearly, as far as this definition of the damping relies only on two independent parameters, it is suitable to express accurately the damping properties of a maximum number of two modes of vibration. In the current case, the analyzed structure can be regarded as a generalized single degree of freedom system and, therefore, it can be effectively characterized by only a single damping parameter. This allows to simplify the assumptions made on the damping matrix by choosing only a stiffness or mass proportional definition.

Therefore, in the FE modelling a mass proportional damping was adopted, defining the constant of proportionality to be introduced in Abaqus as:

$$\alpha = 2\xi_1\omega_{n,1} \tag{6}$$

where ξ_1 and $\omega_{n,\,1}$ are the damping ratio and the first natural frequency of vibration of the beam. The natural frequency of the beam was assessed experimentally by measuring the time lag between two subsequent peaks of the displacement-time curve. Similarly, the damping ratio was estimated starting from the results of the experimental tests, analysing the decay of motion taking place in the elastic impacts (*ITB01 M1 H250 and ITB02 M1 H500*), by measuring the decrement of amplitude occurring between subsequent peaks of the displacement-time history. In fact, assuming that the natural period of vibration of the undamped system ($\omega_{n,\,1}$) is approximated with the period of vibration of the damped system ($\omega_{D,\,1}$) (for low values of damping this assumption leads to accurate results) and considering that the decay of the motion in the free-vibration phase is governed by a decreasing exponential law ($u(t) = \pm Ae^{-\xi\omega_n t}$), it can be demonstrated that the damping ratio can be defined as:

$$\xi_1 = \frac{\delta}{2\pi} \tag{7}$$

where δ is the logarithmic decrement of the displacement amplitude between two subsequent steps (U_n and U_{n+1},as given in Fig. 14) during the free vibration phase following the impact:

$$\delta = \ln\frac{U_n}{U_{n+1}} \tag{8}$$

The obtained values of the first natural frequency and the related damping ratios are summarized in Table 8. It is useful to observe that the first natural frequency is very close to the theoretical value which can be calculated analytically as:

$$\omega_{n,1} = 9.87\sqrt{\frac{EIg}{wL^4}} = 515\ Hz \tag{9}$$

where E is the steel elastic modulus, I is the moment of inertia of the beam and w is the self-weight per unit length. Additionally, it is worth noting that the obtained values of the damping ratio are very close to the 5%, which is the benchmark normally suggested in the design of structures for seismic purposes. A comparison of the signal overlapped to the logarithmic decay curves calculated with different damping ratios is given in Fig. 15.

The material properties of the beam were implemented as true stress-true strain laws, with an isotropic hardening behaviour. The static material laws were defined by simply linearizing the stress-strain results of the coupons previously presented. Conversely, considering that in technical literature there is not a general agreement on the methodology to be adopted to account for the influence of strain rates over the mechanical properties of steel, different hypotheses were

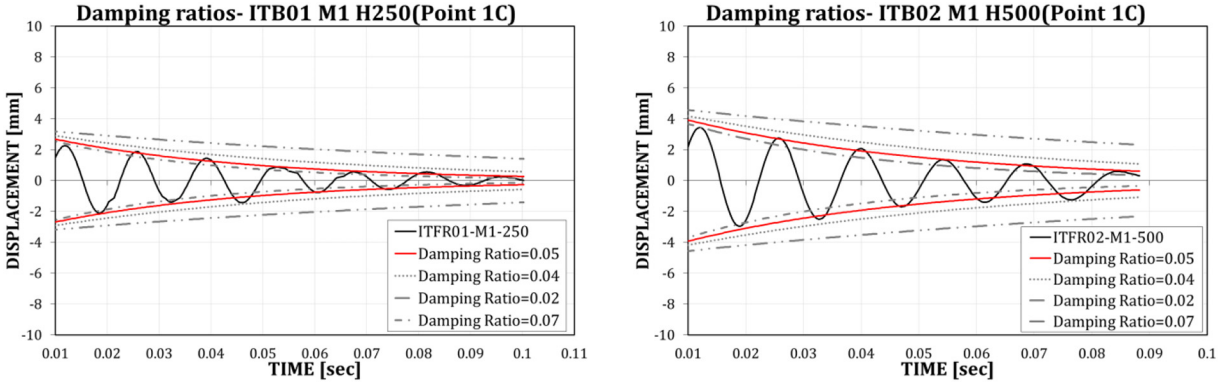

Fig. 15. Signal decay tests ITB01 and ITB02. a) Test ITB01 M1 H250. b) Test ITB02 M1 H500.

made. In particular, four alternative material models were implemented. In a first case, as a benchmark of comparison, steel was modelled neglecting the influence of the strain rate (No Strain Rate-NSR) defining, therefore, the stress-strain law only according to the results of the static tests on the coupons. In the second and third case, the strain rate effect was introduced in the material, considering the Johnson Cook (JC) hardening law and the hardening power law of Cowper and Symonds (CS), respectively. In the last model (DoD) the strain-rate dependency was accounted for according to the codified American approach, by increasing the yield and ultimate stress through the DIF factor as defined in UFC-3-340 [35]. The main features of the adopted material models and procedure of calibration of the experimental coefficients are described in next section.

3.2. Material modelling at high strain rates

One of the most sensitive issues in dynamic problems is related to the material modelling when high strain rates occur ([36–38]). The dependency of the mechanical properties on the rate of deformation is called stain rate sensitivity. When a material undergoes high rates of deformation, the plastic strength may be influenced by a sensitivity which varies from material to material. Even though the influence of the strain rate on the stress-strain behavior of metals is a well-known phenomenon, its modelling involves a large set of variables, such as the crystallographic structure of the material, its chemical composition and the external temperature. Furthermore, especially in complex layouts, the rate of deformation is not constant in space and the behaviour can consistently change according to the considered point of the body in motion. When FE modelling of events like impact, blast, fire, etc. is under concern, the material behavior becomes a key issue due to the high velocities related to transient and time dependent quantities.

The simplest way to account for this phenomenon is by means of the DIF (Dynamic increase factor), which is a factor quantifying the resistance of the material of a structural element in dynamic loading conditions. Practically, the DIF uniformly increases the resistance of the material of a structural member amplifying its static strength in order to account for the dynamic response under high strain rates. Especially in the field of robustness studies under column loss scenario, DIF has been already widely used in literature to account for the dynamic effects in a simplified manner [25,27,39]. The DIF is generally calculated as the ratio between the dynamic and the static strength (Eq. (10)).

$$DIF = \frac{P_{dyn}}{P_{sta}} \tag{10}$$

However, also estimations in terms of displacement and energy are possible, but generally they are less used in structural applications [39]. In most of the cases, the strain rate sensitivity is introduced using empirical and semi-empirical methods. In this work different approaches to account for the strain rate sensitivity in FEM modelling are presented. All the considered options are implemented and compared when applied to the modelling of the drop weight impact tests previously presented.

3.2.1. The Johnson-Cook material law

One of the most used constitutive models for metallic materials under high deformation rates is the Johnson-Cook law (JC) [19,25,40–43], which is defined according to the following expression:

$$\sigma_d = \left(A + B(\varepsilon_p)^n\right)\left(1 + C\ln\frac{\dot{\varepsilon}_p}{\dot{\varepsilon}_0}\right)\left(1-(T^*)^m\right) \tag{11}$$

where σ_d is the dynamic yield stress [MPa], A and B account for the effect of strain hardening; m is the thermal softening factor and $T^* = (T - T_0)/(T_m - T_0)$ where T, T_0 and T_m are respectively the working temperature, room temperature and melting temperature. The expression contains four parameters to be calibrated fitting experimental data.

The second parenthesis of the equation is accounting for the effect of the plastic strain rate, where $\dot{\varepsilon}_p$ is the plastic strain rate, $\dot{\varepsilon}_0$ is the reference static strain rate and C is a constant value. Theoretically the model has four parameters to be determined but, excluding the effect of the temperature and considering that the first parenthesis is representing the static behaviour of steel, the equation can be simply rewritten as follows:

$$\sigma_d = \left(A + B(\varepsilon_p)^n\right)DIF \quad \text{where } DIF = 1 + C\ln\frac{\dot{\varepsilon}_p}{\dot{\varepsilon}_0} \tag{12}$$

In this last expression the dependence of the *DIF* over the strain rate is linear in a logarithmic scale, and the only parameter to be determined is C. The static behaviour of the steel (namely the first parenthesis of Eq. (11)) is modelled as a multilinear law based on a simplification of the true stress true strain curves presented in Table 2, keeping two different material laws for the flange and the beam web.

3.2.2. The Cowper-Symonds material law

Another popular model is the Cowper-Symonds (CS) material law [2,3,44,45], which is based only on two parameters: D and q. These are both related to the deformation rate.

$$\sigma_d = \sigma_s\left(1 + \left(\frac{\dot{\varepsilon}_p}{D}\right)^{\frac{1}{q}}\right) \tag{13}$$

As for the Johnson-Cook law the expression can be rewritten as follows:

$$\sigma_d = \sigma_s DIF \text{ where } DIF = 1 + \left(\frac{\dot{\varepsilon}_p}{D}\right)^{\frac{1}{q}} \tag{14}$$

The influence of the *DIF* in this model is therefore defined by a power function.

3.2.3. The approach of the American code

The U.S. Army in the UFC-3-340 [35] suggests a value of the *DIF* to correct the yield stress (f_y) and the ultimate strength (f_u) of the material to account for the strain rate sensitivity. In particular, in the approach of the UFC, in general, the effect of the strain rate is higher on f_y than f_u as it can be noticed from Fig. 16a. The UFC regulations provide the DIF as dependent on the strain rate through logarithmic expressions (Fig. 16b). In particular, the UFC defines the increase factors for two steel grades: the ASTM A514 ($f_y = 689$ MPa) and the ASTM A36 ($f_y = 248$ MPa).

In this work, in order to assess the accuracy obtained with the proposal of the UFC, reference is made to the values of the *DIF* suggested for the ASTM A36 steel grade, which has a yield stress very similar to the European S275(Fig. 16b).

3.2.4. Calibration of the materials constants

Considering that in this work the dynamic tests on the steel coupons of the impacted beam were not performed, the material parameters defining the strain rate dependence of the stress-strain law were calibrated using other experimental data on similar steel grades. Existing data were used to calibrate the material laws used in this research, the available tests are the outcome of the research project Robust Impact [31] and they were performed by the researchers of the RWTH Aachen University. They regard six tensile static tests on S355 coupons ($\dot{\varepsilon}$= 0.001 1/s considered as the static reference strain rate) and twelve dynamic tests at two speeds, corresponding to two different rates of deformation (six with $\dot{\varepsilon}$=0.5 1/s and six with $\dot{\varepsilon}$=5 1/s). The main results of these tests are summarized in Table 9.

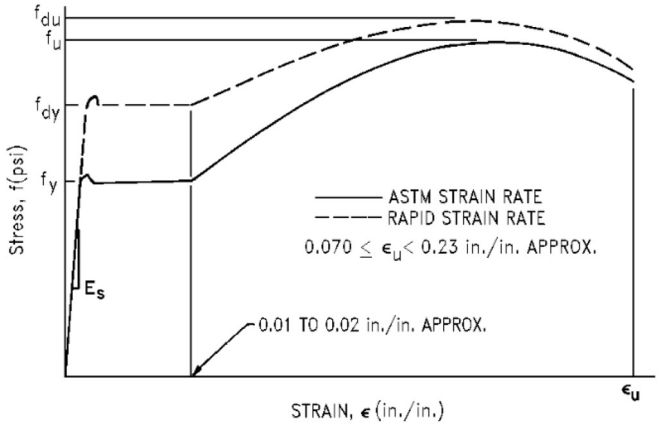

a)

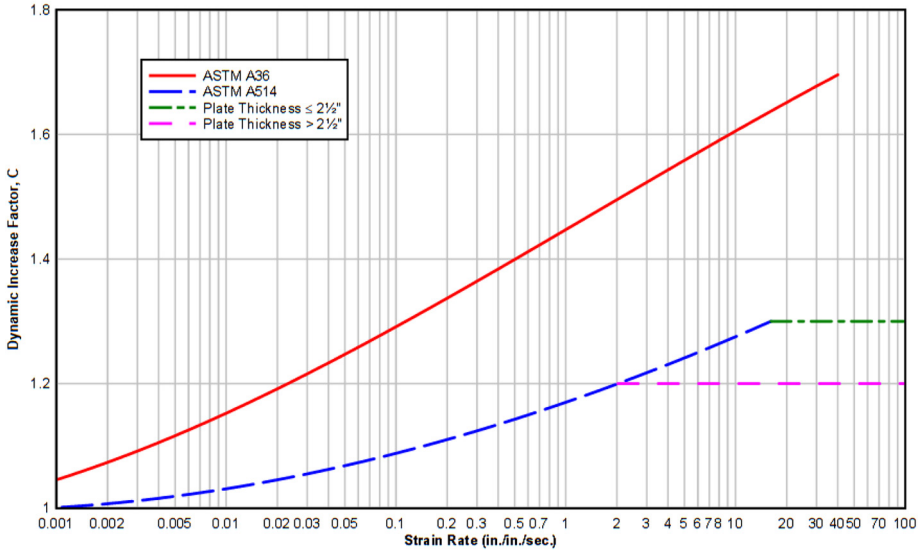

b)

Fig. 16. (a) Typical stress-strain curve; (b) Dynamic increase factor at various strain rates for ASTM A-36 and A-514 steel; retrieved from [35].

Using these test results, the parameters of the semi-empirical laws of Johnson-Cook and Cowper-Symonds were calibrated. The two parameters of the Cowper-Symonds were fitted through a nonlinear least-squares method, obtaining $q = 6.17$ and $D = 8480\ s^{-1}$. Conversely, the Johnson-Cook constant C was defined using the same procedure reported in [19] performing simply a linear regression study. In particular, a value of $C = 0.038$ was found, this results is very similar to the one proposed in [19]. The comparison between the calibrated laws and the experimental data is given in Fig. 17.

4. FE results and discussion

Four FEM models were developed in order to compare the numerical predictions with the experimental results. As aforesaid the four models are identical in terms of geometry, mesh, boundary conditions and contacts but they adopt different constitutive laws for the material definition. In fact, the stress-strain law of the steel composing the beam is introduced, case by case, adopting a different approach to account for the strain rate effect (NRS, JC, CS and DoD).

Table 9
DIF from material coupon tests.

Strain rate ε̇ [1/s]	Test 1 DIF	Test 2 DIF	Test 3 DIF	Test 4 DIF	Test 5 DIF	Test 6 DIF
0.001	1	1	1	1	1	1
0.5	1.17	1.22	1.27	1.26	1.19	1.22
5	1.25	1.25	1.38	1.39	1.27	1.39

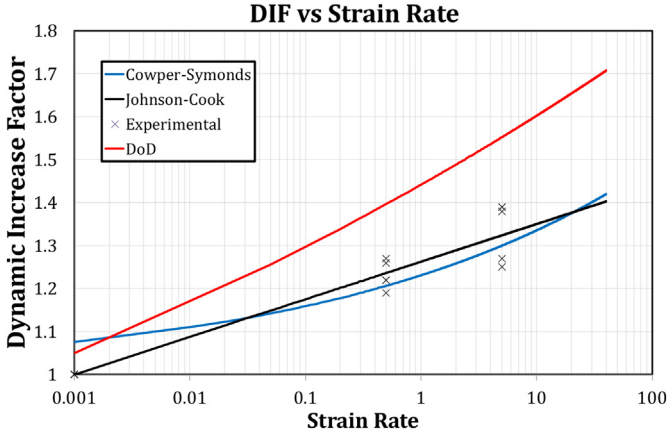

Fig. 17. DIFs comparison.

For the simulations of the tests where the energy associated to the impact was not enough to develop plastic deformations in the beam (ITB01 M1 H250, ITB02 M1 H500 and ITB07 M2 H250), the results of the four models are overlapped and they are all matching accurately the experimental results. The main discrepancies can be found when strain rate starts to increase, hence, when the energy associated to the impact is higher (ITB05 M1 H1000, ITB06 M1 H3000, ITB07 M2 H500 and ITB08 M2 H1000). In these cases, from the point of view of the overall response the four finite element models provide a behaviour similar to the experimental one. Nevertheless, in the various cases significant differences are observed. In fact, while consistently with the test results patterns of plastic deformations are detected under the point of application of the loading, the magnitudes of the maximum stresses and strains are significantly different with the various modelling approaches. Such patterns are delivered in Fig. 18 in terms of PEEQ (equivalent plastic strain) and horizontal strain rate, making reference, as an example, to the case of test ITB06 M1 H3000. From these results, it can be observed that, in general, when the effect of the strain-rate is neglected the plastic deformations are higher. Conversely, due to the overestimation of the actual value of the DIF, with the DoD approach an underestimation of the plastic deformations occurs (Fig. 18c). In terms of strain rate, all the models, except the NSR model predict similar values. In particular, with the NSR model, due to the occurrence of higher strains in the beam, the strain rate is overestimated.

The JC and CS models, from the point of view of the overall prediction of the displacement-time curve are, in general, more accurate (Fig. 19). In fact, as hereinafter reported, they are able to match better the experimental response providing a reliable prediction both of the peak and of the residual displacements. The results in terms of displacement-time curve obtained with the four models are overlapped to experimental ones in Fig. 19 (a-g). From the comparisons it was observed that the eigen-period of the beam is slightly larger in the FE model. This is probably due to the difference between actual and ideal constraints. In fact, the supports are equipped with a couple of threaded

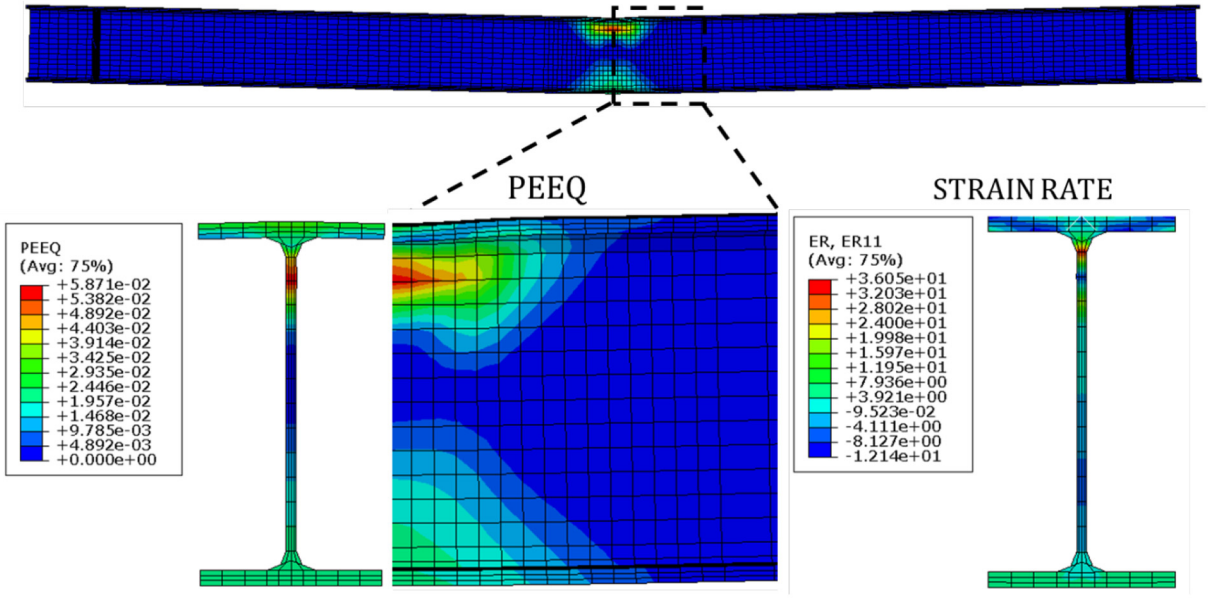

(a) No Strain Rate

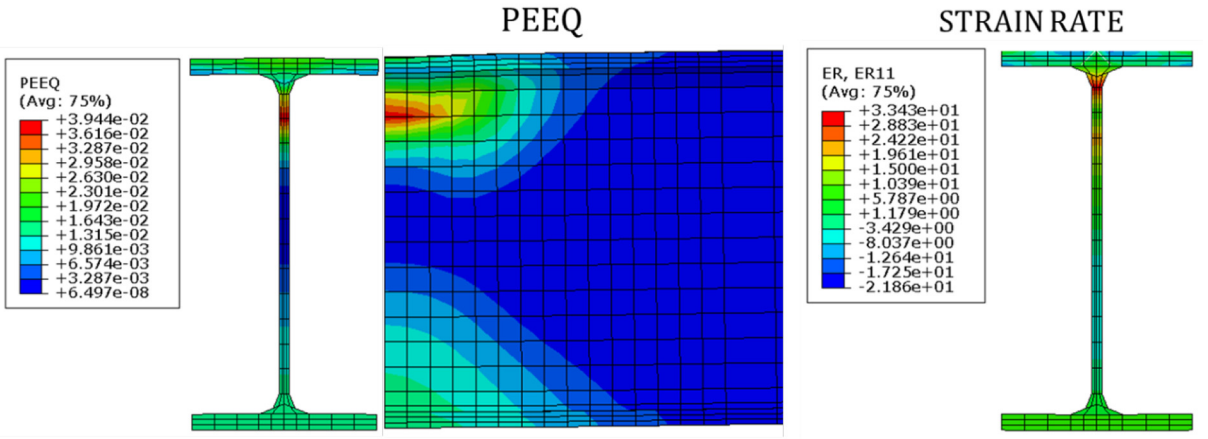

(b) Johnson-Cook

Fig. 18. Comparison between PEEQ and strain rate (ER) values for the different modelling techniques of the test ITB06 M1 H3000: NSR (a), JC (b); DoD (c) and CS (d).

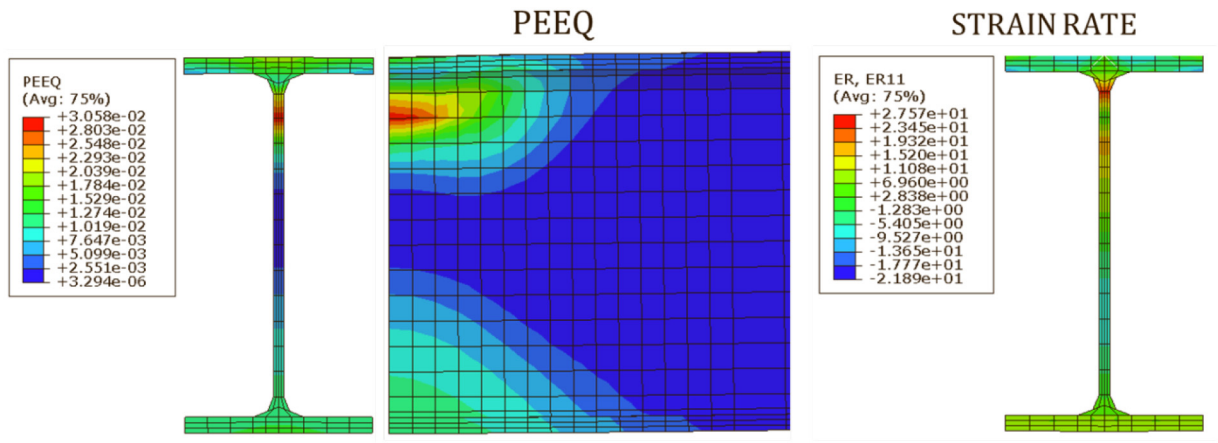

(c) DoD

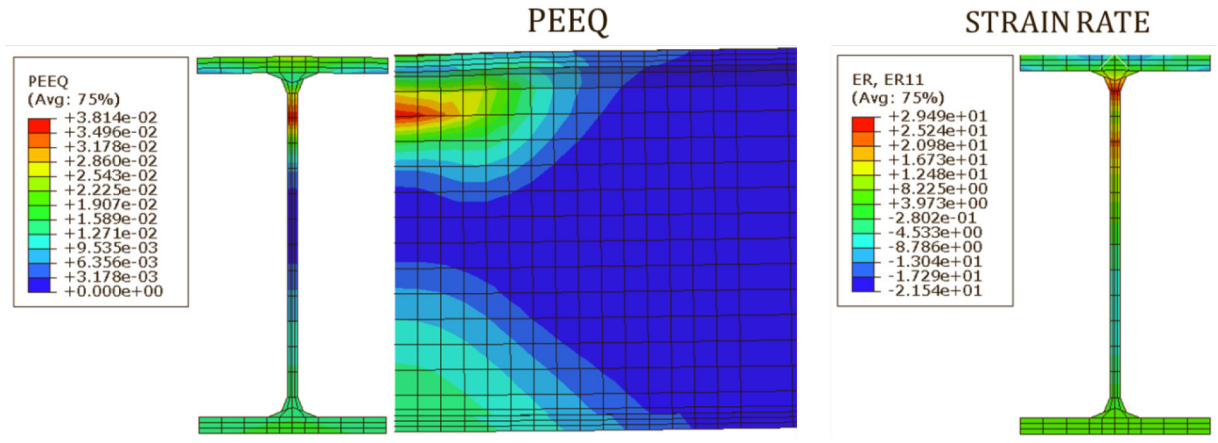

(d) CS

Fig. 18 (*continued*).

bars which provide a small flexural resistance and, additionally, the lateral restraints introduce vertical forces mainly due to the friction arising between the beam and the guides.

In order to compare the results also in terms of forces, the impact force was extracted from the FE model starting from the reaction values at the supports. These values have been filtered through a zero-phase digital filtering procedure in order to reduce the "noise" coming from the vibration of the specimen after the impact. As an example, the original signal and the filtered one are given in Fig. 20 for test IT-B05-M1-H1000-JC, reporting in the same figure the impact force previously estimated through the impulse-momentum theorem. The impact force derived with the FE model is in agreement with the experimental results only for the models JC and CS, while the NSR and DoD model respectively underestimate and overestimate the resistance. The comparisons are given in Tables 10 and 11 and a summary of the force-deflection curves of the inelastic impacts is reported in Fig. 21. In these pictures, the outcomes of the four models are compared with the static prediction of the beam behaviour, which is evaluated simulating a static push-down test by the means of the FEM model previously calibrated with the impact tests.

In the same tables, the experimental results are compared to the FE models also in terms of peak displacements, residual deformations, energy dissipated through plasticity, DIFs and impact forces. Generally, the models DoD and NSR underestimate and overestimate the permanent deformation, respectively. Regarding the peak displacement, the maximum absolute error for inelastic impacts shows that:

- NSR gives an overestimation of +12.8% for ITB09;
- DoD provides an underestimation of −10.17% for ITB06;
- JC underestimates of −4.45% for ITB05;
- CS gives an underestimation of −5.61% for ITB05.

The same comparison can be given in terms of permanent deformation at the end of the test and impact force. Excluding the tests that remained in elastic range, where no permanent deformation appears (ITB01, ITB02 and ITB07), it has been observed that the maximum error is:

- +58.3% for NSR model (ITB08);
- -43.5% for DoD model (ITB05);
- -17.8% for JC model (ITB05);
- -36.3% for CS model (ITB05).

Finally, in terms of impact force, the maximum error of the average force is:

- −25.5% for NSR model (ITB05);
- +15.6% for DoD model (ITB07);

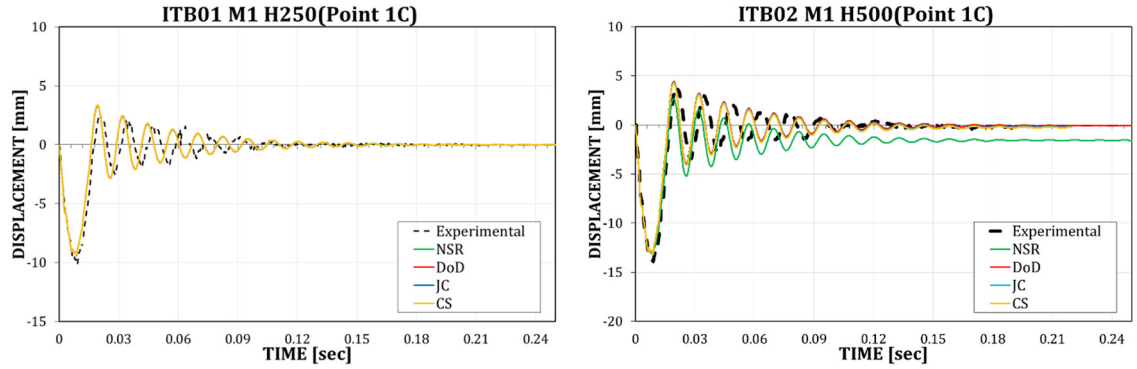

(a)

(b)

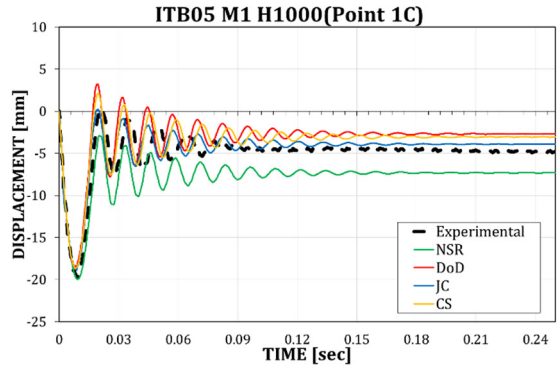

(c)

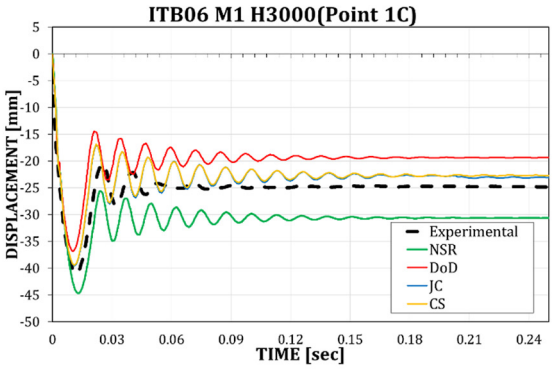

(d)

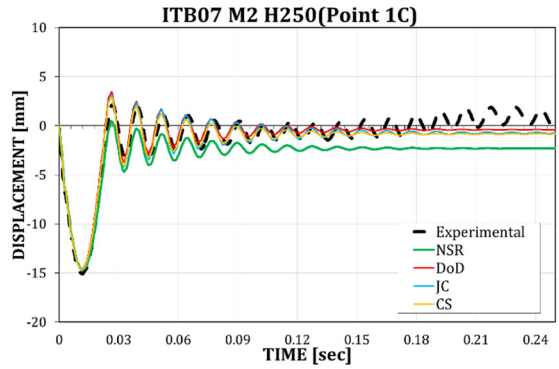

(e)

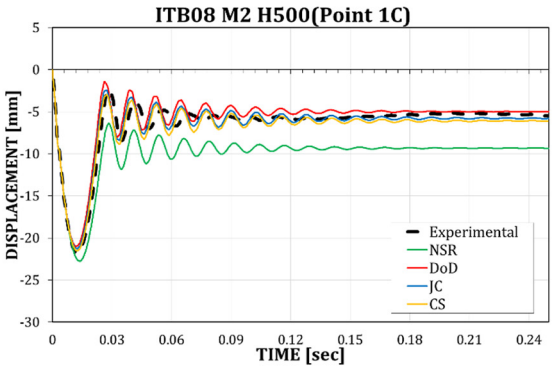

(f)

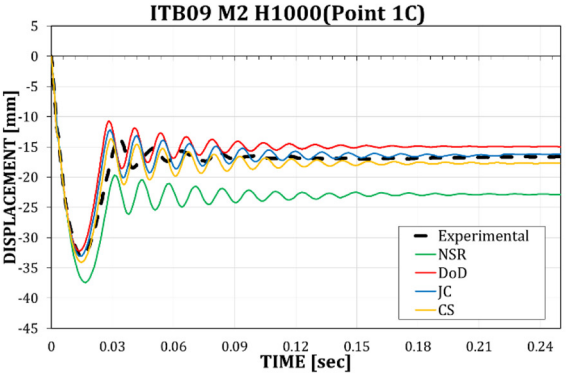

(g)

Fig. 19. Comparison between FEM modelling and experimental tests: (a) ITB01 M1 H250; (b) ITB02 M1 H500; (c) ITB05 M1 H1000; (d) ITB06 M1 H3000; (e) ITB07 M2 H250; (f) ITB08 M2 H500; (g) ITB09 M2 H1000.

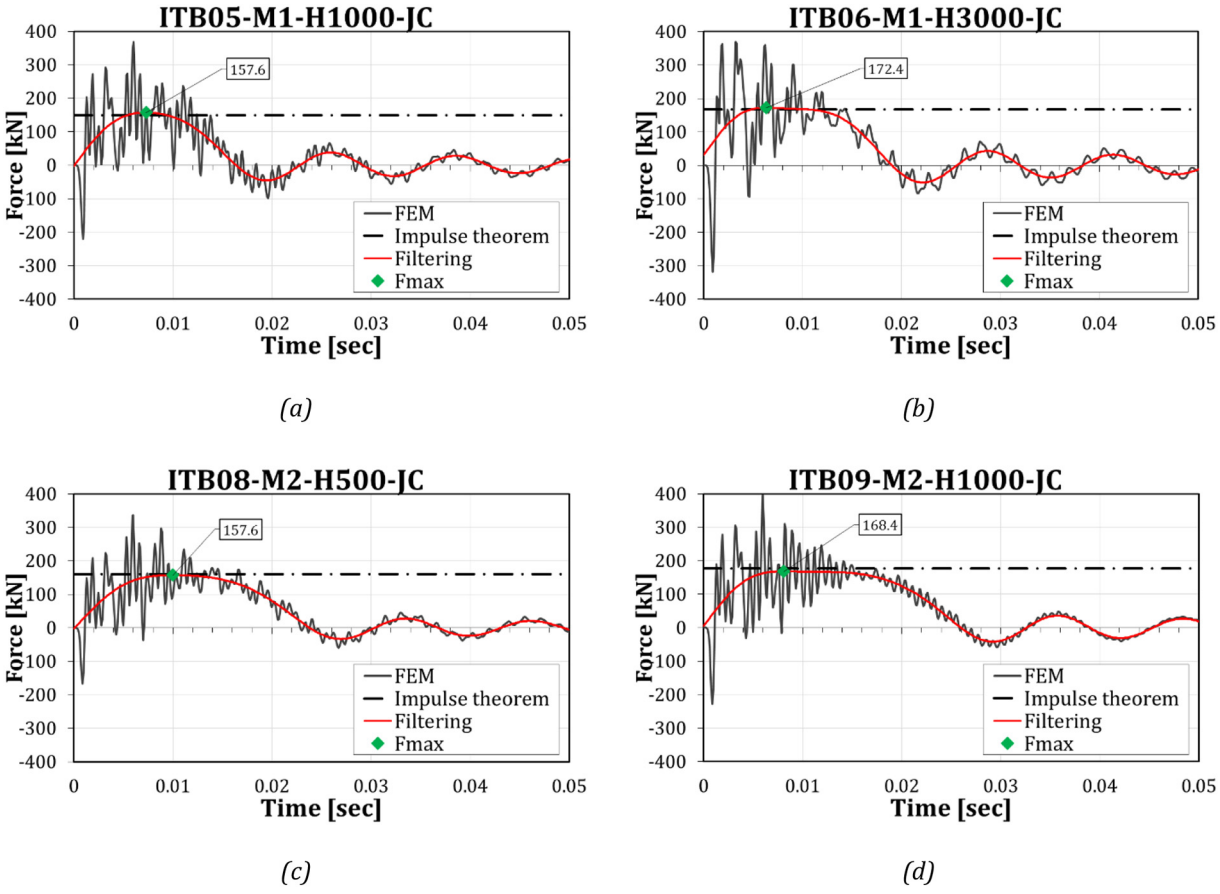

Fig. 20. Filtering of the forces to define the FE force.

Table 10
Results of FEM analyses Mass M1 (all the values are expressed in absolute terms).

	ITB01 M1 H250				ITB02 M1 H500				ITB05 M1 H1000				ITB06 M1 H3000			
	NSR	DoD	JC	CS	NSR	DoD	JC	CS	NSR	DoD	JC	CS	NSR	DoD	JC	CS
$\delta_{peak,FEM}$ [mm]	9.4	9.4	9.4	9.4	13.2	13.2	13.2	13.2	20	18.7	18.9	18.7	44.6	36.8	39.6	39.4
$\delta_{peak,EX}$ [mm]	10.2				13.92				19.77				40.99			
$\delta_{perm,FEM}$ [mm]	≅0	≅0	≅0	≅0	1.57	≅0	0.19	0.26	7.30	2.69	3.91	3.03	30.6	19.3	23.1	22.7
$\delta_{perm,Exp}$ [mm]	≅0				≅0				4.76				25.01			
E_{diss} [J]	2.29	0.05	0.10	0.13	213	13	30.2	42	1043	490.1	675.9	727.8	4679	4010	4257	4309
F_{Stat} [kN]	–				–				137.5				144.2			
$F_{i,FEM}$ [kN]	94	94	94	94	120	130	130	130	111.7	167.0	157.6	154.4	140.1	190.0	172.4	168.6
F_{IT} [kN]	82.82				120.6				149.9				167.4			
DIF_{FEM}	–	–	–	–	–	–	–	–	–	1.21	1.15	1.23	–	1.31	1.20	1.17
DIF_{IT}	–	–	–	–	–	–	–	–	1.09				1.16			

Table 11
Results of FEM analyses Mass M2 (all the values are expressed in absolute terms).

	ITB07 M2 H250				ITB08 M2 H500				ITB09 M2 H1000			
	NSR	DoD	JC	CS	NSR	DoD	JC	CS	NSR	DoD	JC	CS
δ_{peak} [mm]	14.70	14.60	14.67	14.62	22.76	21.01	21.27	21.53	37.39	32.21	33.08	34.06
$\delta_{peak,EX}$ [mm]	15.08				21.74				33.14			
δ_{perm} [mm]	2.31	0.40	0.74	0.84	9.34	4.99	5.80	6.11	22.86	14.96	16.19	17.73
$\delta_{perm,EX}$ [mm]	≅0				5.9				16.78			
E_{diss} [mm]	310.4	62.28	106.2	125.5	1260	795.5	923.1	953.4	3337	2780	2918	2954
F_{Stat} [kN]	–				138.1				141.5			
$F_{i,FEM}$ [kN]	124.8	142.1	139.8	138.7	134.3	170.8	157.6	157.8	142.8	186.2	168.4	168.3
F_{IT} [kN]	122.9				161.2				176.4			
DIF_{FEM}	–	–	–	–	–	1.23	1.14	1.14	–	1.31	1.19	1.19
DIF_{IT}	–	–	–	–	1.17				1.25			

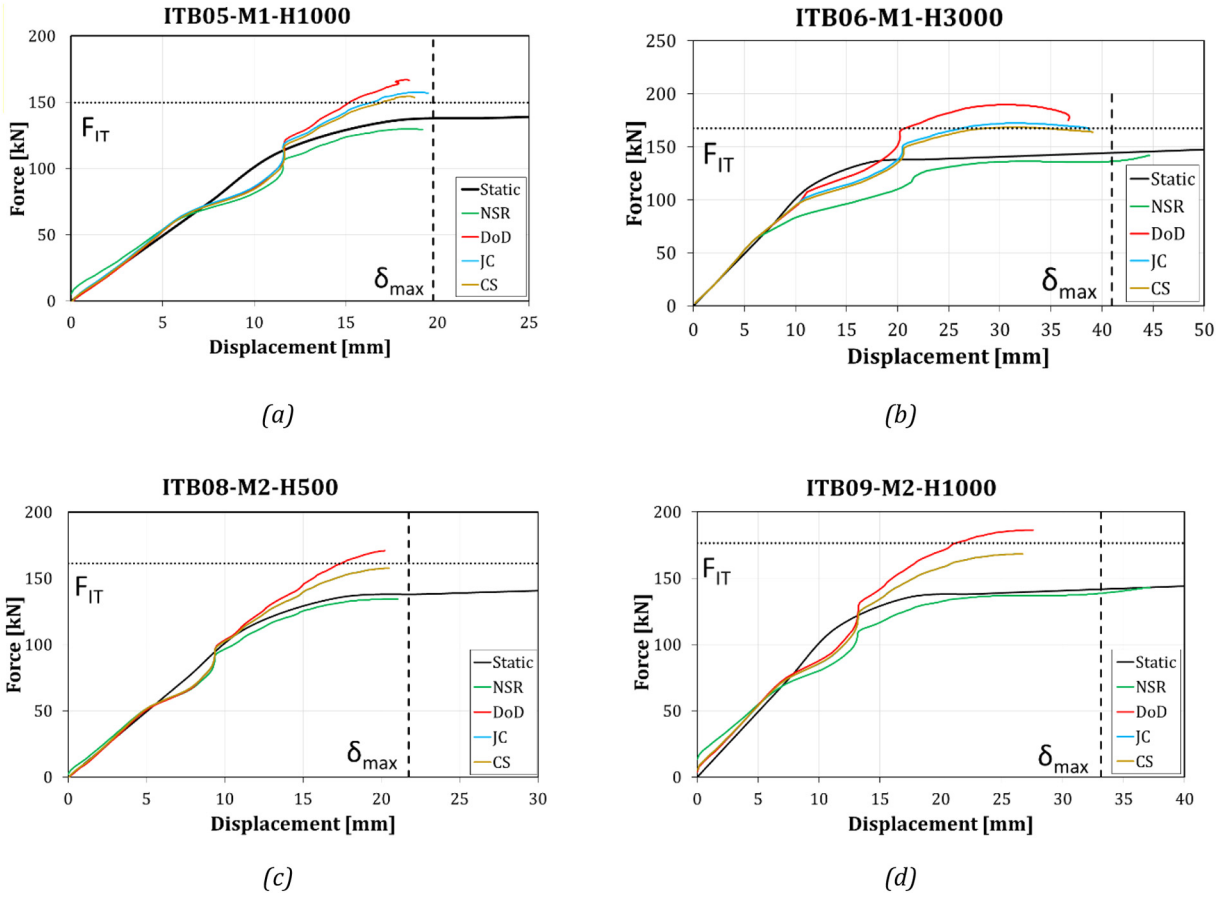

Fig. 21. Force deflection of ITB05 (a), ITB06 (b), ITB08(c) and ITB09(d). Comparison with the static behaviour (solid line) maximum deflection (δ_{max}) and maximum force (F_{IT}).

- +13.7% for JC model (ITB07);
- +13.1% for CS model (ITB01).

Overall, JC and CS are able to estimate with higher accuracy the maximum displacement of the first impact, the permanent deformation and the impact force. Additionally, the NSR and the DoD model do not seem able to predict adequately the value of the permanent deformation. Except from this, the DoD model provides a rather satisfactory accuracy in terms of impact force and maximum displacement and, therefore, it can be still considered reliable if the prediction of the permanent deformation is not of interest.

5. Conclusions

The paper is devoted to the study of the strain rate influence on the response of beams under impact. An experimental campaign on simply supported steel members has been carried out, performing nine impact tests with a drop weight impactor. A particular attention has been devoted to the FE modelling of the material under impulsive loadings considering the possibility to model the stress-strain law through four different approaches: strain rate influence neglected (NSR), Johnson-Cook or Cowper-Symonds material model (JC or CS) and simplified approach suggested by the US regulations (DoD). The main outcomes of the work can be summarized as follows:

- Different methodologies to assess the value of the impact force and, thus the dynamic increase factors of an impacted steel beam have been compared. Both the impulse-momentum theorem and the graphic construction presented in this paper seem to provide a reasonable estimate of the impact forces. Nevertheless, it has to be observed that to apply the impulse-momentum theorem a high frequency of acquisition of the displacements is needed in order to assess with a high level of accuracy the instant of separation of the mass. Conversely, the graphic method is easier to apply because it relies only on the knowledge of the maximum and permanent deflections of the beam;
- The FE can effectively model the response of beams under impacts, provided that the material behavior is adequately characterized considering the influence of the strain rate;
- Neglecting the strain rate influence provides in general an overestimation of the actual displacements and an underestimation of the forces;
- The DIF values proposed by the US Department of Defense do not seem representative of the European steel grades. This was found comparing the results of experiments carried out in [31] with the DIFs suggested for steel ASTM A36. The overestimation of the DIF leads, in general, to an overestimation of the forces and underestimation of the displacements;
- The Cowper-Symonds and Johnson-Cook material models, if properly calibrated on coupon tests carried out at different velocities, provide in general a satisfactory accuracy when compared to the experimental results. The material constants have been determined in this paper basing on the test results given in [19] finding the following parameters: for the Cowper-Symonds model $q = 6.17$ and $D = 8480$, while for the Johnson-Cook model $C = 0.038$;

Acknowledgments

The research activity herein presented has been supported by the European Community with the research grant RFSR-CT-2015-00022. The support of the European Commission within RFCS Research & Innovation is gratefully acknowledged.

Additionally, the authors would like to acknowledge the Institute of Steel Construction of the RTWH Aachen University for providing the data on coupon tests at different speeds.

References

[1] E.L. Grimsmo, A.H. Clausen, M. Langseth, A. Aalberg, An experimental study of static and dynamic behaviour of bolted end-plate joints of steel, Int. J. Impact Eng. 85 (July) (2015) 132–145.

[2] V. Karlos, G. Solomos, Influence of strain rate effects on the analysis of steel sections under blast loads, 8th Hell. Natl. Conf. Steel Struct. Proc., No. September 2001 2014, pp. 1–9.

[3] K. Chen, K.H. Tan, Behaviour of steel and composite beam-column joints subjected to quasi-static and impact loads, Asccs (2018) 29–38.

[4] J.-F. Demonceau, L. Comeliau, L. Hoang Van, J.-P. Jaspart, How can a steel structure survive to impact loading? Numerical and analytical investigations, Open Civ. Eng. J. 11 (2017) 434–452.

[5] A. Santiago, L.S. da Silva, P.V. Real, M. Veljkovic, Numerical study of a steel sub-frame in fire, Comput. Struct. 86 (15-16) (2008) 1619–1632.

[6] P. Barata, C. Rigueiro, A. Santiago, J.P. Rodrigues, Impact loads in steel connections, IABSE Symp. Rep. 100 (4) (2013) 242–249.

[7] A.S. Tzimas, G.S. Kamaris, T.L. Karavasilis, C. Galasso, Collapse risk and residual drift performance of steel buildings using post-tensioned MRFs and viscous dampers in near-fault regions, 8th International Conference on Behavior of Steel Structures in Seismic Areas Shanghai, China, July1-3, 2015, Bull. Earthq. Eng. (2016).

[8] C.Y. Seo, T.L. Karavasilis, J.M. Ricles, R. Sause, Seismic performance and probabilistic collapse resistance assessment of steel moment resisting frames with fluid viscous dampers, Earthq. Eng. Struct. Dyn. 43 (14) (November 2014) 2135–2154, https://doi.org/10.1002/eqe.2440.

[9] T.L. Karavasilis, S. Kerawala, E. Hale, Hysteretic model for steel energy dissipation devices and evaluation of a minimal-damage seismic design approach for steel buildings, J. Constr. Steel Res. 70 (March 2012) 358–367, https://doi.org/10.1016/j.jcsr.2011.10.010.

[10] M. D'Aniello, R. Tartaglia, S. Costanzo, R. Landolfo, Seismic design of extended stiffened end-plate joints in the framework of Eurocodes, J. Constr. Steel Res. 128 (2017) 512–527.

[11] R. Tartaglia, M. Zimbru, M. D'Aniello, S. Costanzo, R. Landolfo, A. De Martino, Numerical investigation on the seismic response of bolted extended stiffened end-plate joints, 8th International Conference on Behavior of Steel Structures in Seismic Areas, 2015.

[12] A.G. Vlassis, B.A. Izzuddin, A.Y. Elghazouli, D.A. Nethercot, Progressive collapse of multi-storey buildings due to sudden column loss-part II: application, Eng. Struct. 30 (5) (2008) 1424–1438.

[13] B.A. Izzuddin, A.G. Vlassis, A.Y. Elghazouli, D.A. Nethercot, OBE, Assessment of Progressive Collapse in Multi-Storey Buildings, Struct. Build. 160 (4) (January 2007) 1424–1438, https://doi.org/10.1680/stbu.2007.160.4.197.

[14] L. Comeliau, B. Rossi, J.-F. Demonceau, Robustness of steel and composite buildings suffering the dynamic loss of a column, Struct. Eng. Int. J. Int. Assoc. Bridg. Struct. Eng. 22 (3) (2012) 323–329.

[15] J.-P. Jaspart, J.-F. Demonceau, L. Comeliau, Robustness of steel and composite buildings suffering the dynamic loss of a column, 7th Natl. Conf. Steel Struct. Proc. 2011, pp. 71–86.

[16] D. Cassiano, M. D'Aniello, C. Rebelo, Parametric finite element analyses on flush end-plate joints under column removal, J. Constr. Steel Res. 137 (2017) 77–92.

[17] European Committee for Standardization, Eurocode 1 – Actions on Structures – Part 1–7: General Actions Accidental Actions, 2006.

[18] Department of Defence, UFC 4–023-03 -Unified Facilities Criteria (UFC) – Design of Buildings to Resist Progressive Collapse, 2016.

[19] J. Ribeiro, A. Santiago, C. Rigueiro, P. Barata, M. Veljkovic, Numerical assessment of T-stub component subjected to impact loading, Eng. Struct. 106 (1 January 2016) 450–460.

[20] T. Sabuwala, D. Linzell, T. Krauthammer, Finite element analysis of steel beam to column connections subjected to blast loads, Int. J. Impact Eng. 31 (7) (2005) 861–876.

[21] R. Rahbari, A. Tyas, J.B. Davison, E.P. Stoddart, Web shear failure of angle-cleat connections loaded at high rates, JCSR 103 (2014) 37–48.

[22] E.L. Grimsmo, A.H. Clausen, A. Aalberg, M. Langseth, A numerical study of beam-to-column joints subjected to impact, Eng. Struct. 120 (February 2017) (2016) 103–115, https://doi.org/10.1016/j.engstruct.2016.04.031.

[23] E.L. Grimsmo, A.H. Clausen, A. Aalberg, M. Langseth, Beam-to-column joints subjected to impact loading, Nord. Steel Constr. Conf., No. November (2015).

[24] B. Yang, H. Wang, Y. Yang, S.B. Kang, X.H. Zhou, L. Wang, Numerical study of rigid steel beam-column joints under impact loading, J. Constr. Steel Res. 147 (2018) 62–73.

[25] A. Al-Rifaie, Z.W. Guan, S.W. Jones, Q. Wang, Lateral impact response of end-plate beam-column connections, Eng. Struct. 151 (November) (2017) 221–234.

[26] H.C. Yim, T. Krauthammer, Load-impulse characterization for steel connection, Int. J. Impact Eng. 36 (5) (2009) 737–745.

[27] Q. Fu, et al., Dynamic analyses of bolted-angle steel joints against progressive collapse based on component-based model, JCSR 117 (2016) 161–174.

[28] H. Wang, B. Yang, X.H. Zhou, S.B. Kang, Numerical analyses on steel beams with fin-plate connections subjected to impact loads, J. Constr. Steel Res. 124 (September 2016) 101–112.

[30] J.-F. Demonceau, H. Vanvinckenroye, M. D'Antimo, V. Denoel, J.-P. Jaspart, Beam-to-column joints, column bases and joint components under impact loading, CE/Papers 1 (2–3) (Sep. 2017) 3890–3899.

[31] Robust Impact Design of Steel and Composite Building Structures – ROBUSTIMPACT, Final Report, Grant Agreement Number RFSR-CT-2012-00029, 2015.

[32] P. Eyckens, et al., Strain evolution in the single point incremental forming process: digital image correlation measurement and finite element prediction, Int. J. Mater. Form. 4 (2011) 55–71.

[33] M. Latour, G. Rizzano, M. D'Antimo, J.F. Demonceau, J.P. Jaspart, V. Armenante, Bearing strength of shear connections for tubular structures: An analytical approach, Thin-Walled Struct. 127 (2018) 180–199;
M. D'Antimo, J.F. Demonceau, J.P. Jaspart, M. Latour, G. Rizzano, Experimental and theoretical analysis of shear bolted connections for tubular structures, J. Constr. Steel Res. 138 (2017) 264–282.

[34] M. D'Antimo, M. Zimbru, M. D'Aniello, J.F. Demonceau, J.P. Jaspart, R. Landolfo, Preliminary finite element analyses on seismic resistant FREE from DAMage beam to column joints under impact loading, Key Eng. Mater. 763 (Feb. 2018) 592–599.

[35] UFC 3-340-02, Structures to resist the effects of accidental explosions, Struct. Congr. 2011, No. May 2005 2008, p. 1867.

[36] N. Jones, Structural Impact, Cambridge University Press, 1989.

[37] G.R. Johnson, W.H. Cook, Fracture characteristics of three metals subjected to various strains, strain rates, temperatures and pressures, Eng. Fract. Mech. 21 (1) (Jan. 1985) 31–48.

[38] M. Stopel, D. Skibicki, Determination of Johnson-Cook model constants by measurement of strain rate by optical method, AIP Conf. Proc. 1780 (2016).

[39] C. Liu, K. Hai, T. Tat, C. Fung, Dynamic Behaviour of Web Cleat Connections Subjected to Sudden Column Removal Scenario, 2013.

[40] J. Ribeiro, A. Santiago, C. Rigueiro, L.S. Da Silva, Analytical model for the response of T-stub joint component under impact loading, J. Constr. Steel Res. 106 (2015) 23–34.

[41] A.V. Sobolev, M.V. Radchenko, Use of Johnson–Cook plasticity model for numerical simulations of the SNF shipping cask drop tests, Nucl. Energy Technol. 2 (4) (2016) 272–276.

[42] Qin Fei, An Tong, Chen Na, Strain rate effect and Johnson-Cook models of lead-free solder alloys, 2008 International Conference on Electronic Packaging Technology & High Density Packaging 2008, pp. 1–7.

[43] J. Ribeiro, A. Santiago, C. Rigueiro, Material modelling of tensile steel component under impulsive loading, Int. J. Struct. Integr. 7 (2) (2016) 323–342, https://doi.org/10.1108/IJSI-05-2014-0026.

[44] M. Avalle, G. Belingardi, M. Gamarino, An inverse method for the identification of strain-rate sensitivity parameters of sheet steels, Struct. Mater. 15 (2004) 13–22.

[45] L. Chang, T.K. Hai, F.T. Ching, A. Tyas, Numerical simulation of steel bolted beam-column connections subjected to dynamic loading, 3rd International Workshop on Performance, Protection and Strengthening of Structures under Extreme Loading, PROTECT2011, 2011.

[46] M. Latour, G. Rizzano, A. Santiago, L. Simões da Silva, Experimental response of a low-yielding, self-centering, rocking column base joint with friction dampers, Soil Dyn. Earthq. Eng. 116 (2019) 580–592.

[47] A.B. Francavilla, M. Latour, V. Piluso, G. Rizzano, Bolted T-stubs: A refined model for flange and bolt fracture modes, Steel Compos. Struct. 20 (2) (2016) 267–293.